Environ Monit Assess (2018) 190: 8
https://doi.org/10.1007/s10661-017-6320-9

Multiple timescale analysis of the urban heat island effect based on the Community Land Model: a case study of the city of Xi'an, China

Meiling Gao · Huanfeng Shen · Xujun Han · Huifang Li · Liangpei Zhang

Received: 9 June 2017 / Accepted: 20 October 2017 / Published online: 6 December 2017

Abstract Urban heat islands (UHIs) are the phenomenon of urban regions usually being warmer than rural regions, which significantly impacts both the regional ecosystem and societal activities. Numerical simulation can provide spatially and temporally continuous datasets for UHI analysis. In this study, a spatially and temporally continuous ground temperature dataset of Xi'an, China was obtained through numerical simulation based on the Community Land Model version 4.5 (CLM4.5), at a temporal resolution of 30 min and a spatial resolution of 0.05° × 0.05°. Based on the ground temperature, the seasonal average UHI intensity (UHII) was calculated and the seasonal variation of the UHI effect was analyzed. The monthly variation tendency of the urban heat stress was also investigated. Based on the diurnal cycle of ground temperature and the UHI effect in each season, the variation tendencies of the maximum, minimum, and average UHII were analyzed. The results show that the urban heat stress in summer is the strongest among all four seasons. The heat stress in urban areas is very significant in July, and the UHII is the weakest in January. Regarding the diurnal cycle of UHII, the maximum always appears at 06:30 UTC to 07:30 UTC, while the minimum intensity of the UHI effect occurs at different times in the different seasons. The results of this study could provide a reference for policymakers about how to reduce the damage caused by heat stress.

Keywords Urban heat island · CLM4.5 · Diurnal variation · Multiple timescale

M. Gao · H. Shen (✉) · H. Li
School of Resource and Environmental Sciences,
Wuhan University, Wuhan, Hubei, 430079, China
e-mail: shenhf@whu.edu.cn

X. Han
Chongqing Key Laboratory of Karst Environment,
School of Geographical Sciences, Southwest University,
Chongqing, 400715, China

L. Zhang
The State Key Laboratory of Information Engineering
in Surveying, Mapping and Remote Sensing,
Wuhan University, Wuhan, Hubei, 430079, China

Introduction

Urban heat islands (UHIs) are the phenomenon of urban regions usually being warmer than their surroundings (Magee et al. 1999; Rizwan et al. 2008; Voogt and Oke 2003). In recent years, the UHI effect has been aggravated with the process of urbanization, industrialization, and the increase of the urban population (Zhang et al. 2010). Researchers have indicated that the heat absorption ability of impervious surfaces (Chen et al. 2006; Yuan and Bauer 2007), the heat release from factories, vehicles, and human activities (Magee et al. 1999; Rizwan et al. 2008; Iodice and Senatore 2012, 2013), and even air pollution are the driving factors of the UHI effect (Bowling 1983; Cao

et al. 2016). The study of UHIs is crucial to urban residential activities and the human living environment. The intensity of UHI (UHII) was always used to quantify the effect of urban heat stress. Adopting an indicator like UHII can provide a convenience way to identify the variation of UHI. To calculate the UHII, temperature datasets can be obtained through a variety of means, such as in-situ measurements, retrieval from remotely sensed images, and simulation by numerical models (Meehl and Tebaldi 2004; Oleson et al. 2011; Voogt and Oke 2003).

Although air temperature measurements from monitoring stations have a higher accuracy in the observation time (Chow and Roth 2006), their application in UHI studies is limited by the sparse distribution of the monitoring stations, especially at a regional or global scale (Aikawa et al. 2007; Shen et al. 2016a; Iodice and Senatore 2015). In addition, the problem of how to use point measurements to represent a region is also a daunting challenge. Even with a dense network of monitoring stations, the uneven distribution of the stations can lead to some serious shortcomings for the interpolation approach (Ho et al. 2016). In order to compensate for the disadvantage of in-situ observations in spatial continuity, land surface temperature (LST) retrieved from remotely sensed images has been widely used to study the surface UHI effect. Remotely sensed images play an important role in the study of UHIs (Weng 2009; Weng and Fu 2014; Xu 2009), as a result of their characteristics of wide coverage, convenient acquisition, and less influence from the ground. Meanwhile, remote sensing data are more widely used with the advanced processing technologies in recent years (Shen et al. 2015, 2016b). However, the revisit cycle of the polar orbiting satellites is the limiting factor which determines the temporal resolution of UHI studies (Zakšek and Oštir 2012). For instance, the Moderate Resolution Imaging Spectroradiometer (MODIS) LST product has a finer-scale temporal resolution than the data from other sensors such as Landsat, but MODIS cannot provide data more than four times a day (Wan 2014; Wan et al. 2004). Several previous studies have investigated the diurnal changes of UHIs (Du et al. 2016; Tran et al. 2006) based on MODIS LST, but the temporal resolution of four observations per day is far from enough to analyze the diurnal cycles of LST and UHIs. Meanwhile, although geostationary satellites such as the Geostationary Operational Environmental Satellites (GOES) have the capability of making repeated observations over a given area (Sun and Pinker 2003), the observation conditions of remote sensors are always hampered by cloud cover, which, to a large degree, limits their capability in practice, especially in the continuous spatial scale studies.

Spatially and temporally continuous temperature datasets can be simulated by a relevant climate model or land surface model (LSM) (Miao et al. 2009; Ohashi et al. 2007; Oleson et al. 2015; Smith et al. 2007). However, the precision of the model output is easily affected by the input dataset and the model uncertainties. To validate the model's applicability, simulation experiments can be optimized by the use of more suitable input datasets, and the simulation results can be compared with in-situ or remotely sensed observations. A number of previous studies have used air temperature data from the Weather Research and Forecasting (WRF) model to analyze UHIs (Giannaros et al. 2013; Salamanca et al. 2012). Although UHI effects based on sub-surface, surface, and air temperatures are related, the processes involved in their genesis and temporal dynamics are distinct (Oke 1995; Saaroni et al. 2000). Existing research has shown that surface temperature is poorly correlated with air temperature (Ho et al. 2016). Compared to studies of UHIs based on air temperature, studies of UHIs based on surface temperature or ground temperature are rare. More and more land models are being developed, but most of them ignore the urban land-cover class, because of the small percentage of the urban areas. The Community Land Model (CLM) is the land component of the Community Earth System Model (CESM), and the urban parameterization scheme of the CLM (CLMU) has been adopted in this land model since version 4.0, which provides us with the opportunity to study UHIs (Oleson et al. 2010a). Although the model has been used to study UHIs in several previous studies (Cao et al. 2016; Oleson et al. 2015; Zhao et al. 2014), few studies have focused on multiple timescale analysis of the UHI effect in China.

The city of Xi'an, as the economic hub of the northwestern part of China, is located in a semi-arid zone. The heat environment of Xi'an is of great importance to the regional climate. Thus, the city of Xi'an was selected as the study region. In order to obtain spatially and temporally continuous ground temperature,

the latest version of the CLM which contains the urban model was selected as the numerical model in this study. A numerical simulation experiment based on CLM4.5 was conducted, and the simulation results were compared with MODIS LST datasets. The multiple timescale analysis of the UHI effect was then undertaken.

The objective of this study was to analyze the multiple timescale variation of the UHI effect, especially the diurnal cycle of UHII in different seasons, based on the spatially and temporally continuous ground temperature simulated by CLM4.5.

Materials and methods

Study region

Xi'an (N 33°42′ ∼ 34°44′30″, E 107°40′ ∼ 109°49′) is the capital city of Shaanxi province, China, with an administrative area of 9983 km^2. Figure 1 shows the administrative map of the city of Xi'an. The city is located in the middle of the Yellow River basin, which lies in the intermediate belt between the humid climate of the southeastern coastal area and the dry climate of the northwestern inland area. The climate of Xi'an

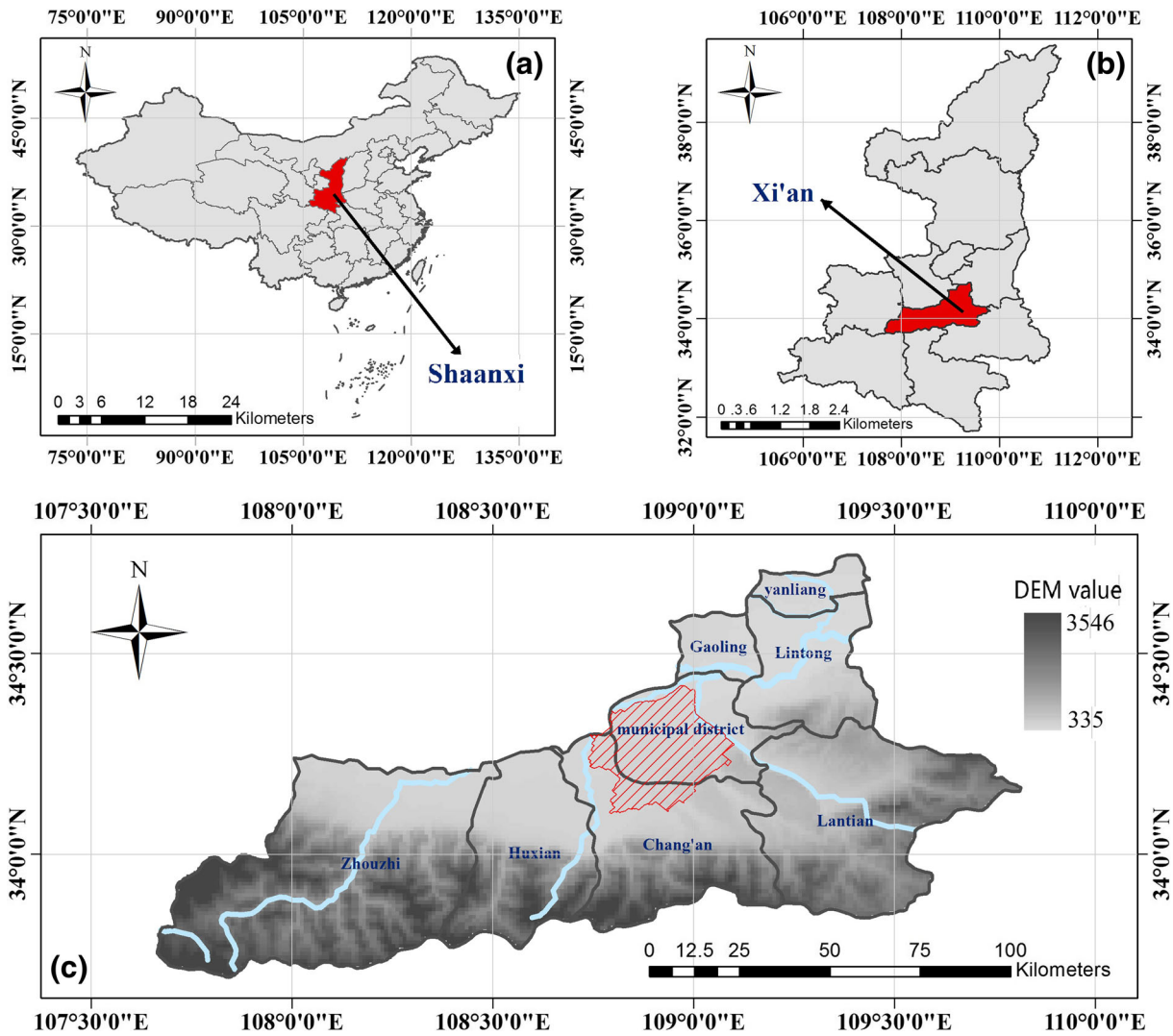

Fig. 1 The study region. **a** The location of Shaanxi province in China. **b** The location of the city of Xi'an in Shaanxi province. **c** Administrative map of the city of Xi'an (the red hatched region is the urban region, and the other areas are regarded as the rural region)

belongs to the warm temperature zone half moist monsoon climatic region, which is mainly affected by local topography. Xi'an has four distinct seasons of dry-wet and cool-warm. In spring, the temperature rises quickly, with dry air and multi-winds, while the climate becomes hot with high temperatures and strong sunshine in summer. There is then a mild and humid period with a higher frequency of rainfall in autumn, and the winter is characterized by cold and dry weather, along with less rain and some snow. Qinling Mountain is located to the south of Xi'an, and there is a warming effect when the air flows from the south across the mountain. The municipal districts of Xi'an, Huxian, and Lantian counties have more sunshine than Gaoling, Chang'an, Lintong, and Zhouzhi counties. In addition, the city is affected by haze, for more than 10 days on average, in the autumn and winter every year.

Ground temperature simulation

The Community Earth System Model (CESM) developed by the National Center for Atmospheric Research (NCAR) consists of various components, including an atmospheric model, a land model, a river-runoff model, an ocean model, a sea-ice model, a land-ice model, and an ocean-wave model. The Community Land Model (CLM) is the land model embedded in the CESM (Gent et al. 2011; Lawrence et al. 2011). The first version of the CLM was proposed in 1998. The model has since been continuously developed to improve the simulation capacity. Although the CLM was provided in the CESM since version 4.0, this implies that the model should be run in the structure of the CESM, but it can in fact be conducted off-line (run without the atmospheric model). It is worth noting that an urban parameterization scheme for the CLM (CLMU) has been integrated in CLM4.0, to distinguish between urban and rural, which makes it possible to study UHIs based on CLM/CLMU (Oleson et al. 2010a, b). Compared with CLM4.0, CLM4.5 released in 2013 contains several modified parameterization schemes, to improve the model simulation accuracy and reduce the simulation bias. The canopy processes, the hydrological cycles, the new snow cover fraction parameterization, the lake model, the soil carbon and nitrogen pool structure, the biogenic volatile organic compounds model, and many other aspects have been revised in CLM4.5 (Oleson et al. 2013). It is worth mentioning that multiple urban density classes are adopted in the urban model in CLM4.5, which results in a better performance in ground temperature simulation contrast between urban and rural areas.

To simulate the ground temperature in the city of Xi'an and then analyze the UHI effect, numerical experiments based on CLM4.5 were conducted in this study. A flowchart of the experimental procedure is shown in Fig. 2. The CLM4.5 input requirements contain four aspects: (1) Atmospheric forcing datasets. The model can be forced in two ways, i.e., an online and an off-line mode. The first method is coupled

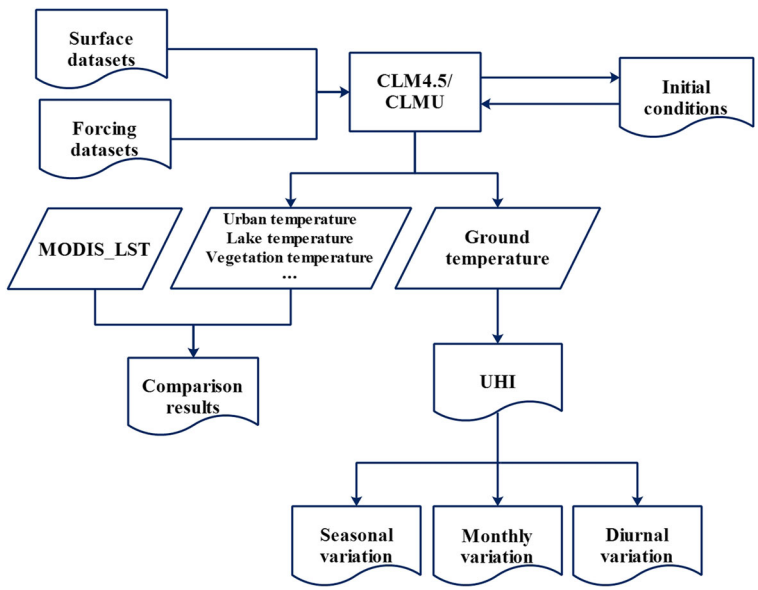

Fig. 2 Flowchart of the experimental procedure based on CLM4.5

with an atmospheric model, such as the Community Atmosphere Model (CAM) in CESM, and the second method forces the land model with a meteorological dataset. The off-line mode was selected in this study. The default forcing dataset of CLM4.5 is the CRUNCEP forcing dataset, which provides 110-year long-term meteorological data. The spatial resolution of CRUNCEP is 0.5° × 0.5° and the temporal resolution is 6-hourly (Viovy 2011). To obtain simulation output datasets in a finer-scale temporal and spatial resolution, the China Meteorological Forcing Dataset (CMFD) developed by the Institute of Tibetan Plateau Research of the Chinese Academy of Sciences (ITPCAS) was chosen as the forcing dataset in the experiments (Chen et al. 2011; Yang et al. 2010). This dataset contains seven meteorological variables: near-surface air temperature, air pressure, specific humidity, wind speed, downward shortwave radiation, downward longwave radiation, and precipitation rate. This dataset covers China for the temporal period of 1979 to 2010, with a spatial resolution of 0.1° × 0.1° and a 3-hourly temporal resolution. (2) Parameters and physical constants. In the experiments, we adopted the default setup. (3) The surface dataset developed by Jackson et al. (2010) was selected as the surface dataset in CLM4.5. (4) Initialization conditions. For the purpose of obtaining a stable and reasonable initial condition, a 10-year numerical simulation experiment based on CLM4.5 was run from March 3, 1993, to February 28, 2003, every 30 min at a spatial resolution of 0.05° × 0.05° as a spinning-up stage. The final output variables of this stage were regarded as the initialization conditions for the model simulation period.

After the preparation of the model input datasets and the basic setup, the model simulation stage was conducted. At this stage, the model was run every 30 min from March 01, 2003 to February 29, 2004, with a special resolution of 0.05° × 0.05° for the simulation period. It is worth noting that a nested sub-grid hierarchy, as shown in Fig. 3, was adopted to represent the spatial heterogeneity when the model was run. Each grid cell (0.05° × 0.05°) consisted of a series of land units, and a number of columns belong to a land unit; meanwhile, there were multiple plant function types (PFTs) in each column. In the numerical simulation experiment of ground temperature in the city of Xi'an, the first sub-grid level was the land units, which were set as lake, urban, and vegetation, according to the land-use type of Xi'an. However, the CLMU only works for urban land units. Within each urban land unit, there were three urban density classes, i.e., tall building district (TBD), high-density (HD) urban area, and medium-density (MD) urban area. Five columns were included in each urban land unit, i.e., roof, sunlit walls, shaded walls, pervious floor, and impervious floor. In the urban land units, a street canyon was the basic simulation unit, and the street canyon geometry was described by the building height (H) and street width (W) (Oleson et al. 2010a, 2013).

For the roof, wall, road, and soil temperature calculation, the following heat diffusion equation is used in CLM4.5:

$$c\frac{\delta T}{\delta t} = -\frac{\delta}{\delta z}\left(\lambda\frac{\delta T}{\delta z}\right) \quad (1)$$

Where T is the temperature, c is the volumetric heat capacity ($Jm^{-3}K^{-1}$), t is the time (s), z is the

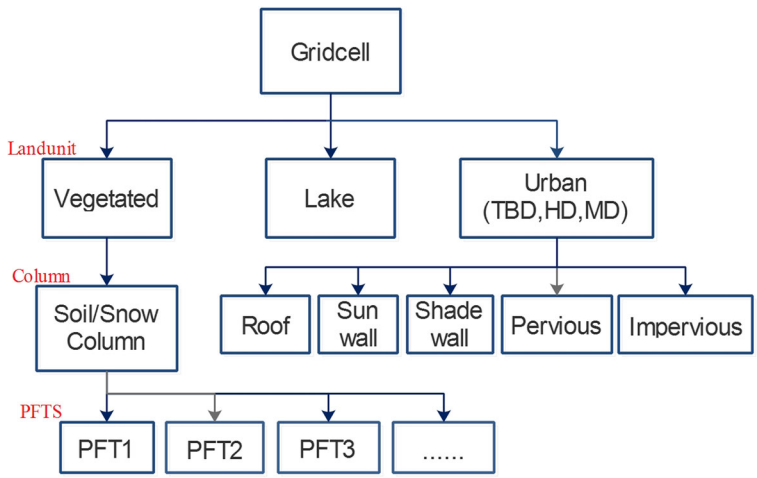

Fig. 3 Sub-grid hierarchy in the simulation experiment

vertical depth (m), and λ is the thermal conductivity ($Wm^{-1}K^{-1}$). For the different types of land surfaces, the different solutions of this equation were adopted in the model simulation.

From the simulation results, ground temperature, urban ground temperature, rural ground temperature, vegetation temperature, and soil temperature in each grid cell could be obtained. It is worth noting that the urban ground temperatures are based on the model sub-grid hierarchy definition. As mentioned in Fig. 3, each grid cell includes urban and other land units; thus, the output urban ground temperatures are only for the urban land units. In other words, calculation of the UHII in this study followed the common definition of urban and rural areas, as shown in Fig. 1, and the model running and output were in accordance with the default definition of the land surface nested sub-grid structure in CLM4.5, as shown in Fig. 3.

The MOD11C1 and MYD11C1 MODIS LST products were selected as reference datasets to compare with the simulation results based on CLM4.5. The MODIS LST products are obtained by the Terra or Aqua satellites at a view angle. This means that the MODIS LST is the "skin temperature" of the land surface, i.e., a mixture of ground temperature and vegetation temperature. In our study area, there were three main land-use classes as shown in Fig. 3, i.e., lake, urban, and vegetation. In the lake and urban land units without vegetation cover, the LST is equal to the ground temperature of the lake and urban units, while in the vegetation land unit, the ground temperature and vegetation temperature should be converted to a mixture temperature, as viewed in the MODIS sensor angle. In this study, an observation operator named the two-source framework (TSF) was used to transform the simulated ground temperature based on CLM4.5 to LST seen as the MODIS view angle in each grid cell. Details of the observation operator can be found in previous documents (Anderson et al. 2005; Kustas and Anderson 2009). On this basis, the simulated LST obtained by CLM4.5 and MODIS LST were compared.

UHI calculation

After obtaining the temperature datasets based on CLM4.5, the ground temperature of each grid cell was used to calculate the mean temperature of the urban and rural areas, to further calculate the UHI effect. The red hatched region shown in Fig. 1 was regarded as the urban region in the UHI calculation. The urban region was extracted from the Landsat image of Xi'an in 2003 under the rule of extracting the impervious edge which contains the dominant urban areas. The other areas were considered as the rural region. The UHII was calculated by the mean ground temperature based on the urban and rural areas described in Fig. 1.

There are several ways to calculate the intensity of UHI. Some was based on the sample data (Zhao et al. 2014; Cao et al. 2016) and some used the average of all the valid data (Zhang et al. 2017; Shen at al. 2016a; Haashemi et al. 2016). In order to avoid the random errors in sample process, the calculation method based on the difference in average ground temperature between the urban and rural areas was adopted. The following equation explains the calculation method of UHII used in this study:

$$UHII = T(urban) - T(rural) \quad (2)$$

Where $T(urban)$ is the average ground temperature in the urban area; meanwhile, the rural average ground temperature is represented as $T(rural)$.

The definitions of the seasons are as follows: spring is from March to May, while summer is the following three months, autumn is from September to November, and winter is from December to February in the next year. The monthly average UHII at every half hour was calculated by the ground temperature of every 30 min in a day during this month. More specifically, Fig. 4 shows the calculation method for the monthly average UHII in March. Similarly, the seasonal average UHII was calculated at every 30 min in a day during the season. In other words, we calculated the average diurnal UHII at monthly and seasonal scales. In the following, based on the statistical results, the seasonal and monthly variations of UHII are analyzed, and then the diurnal cycle characteristics of the ground temperature and urban heat stress are discussed.

Results

Comparison between the LST based on the CLM and MODIS

Figure 5 shows the relationship between CLM LST and MODIS LST. In this study, we only employed

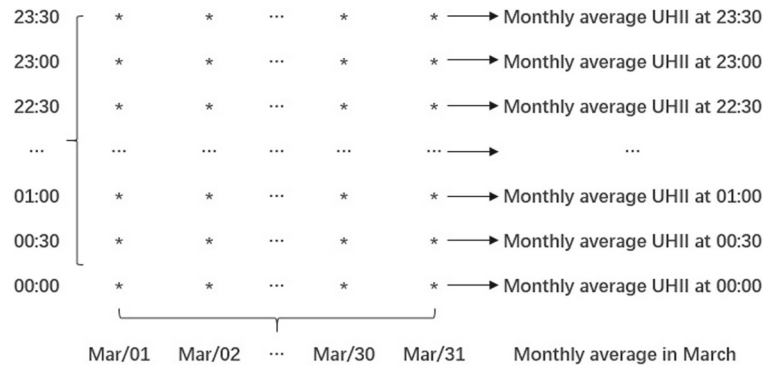

Fig. 4 Calculation illustration for the monthly average UHII (taking the March average UHII as an example)

good-quality MODIS LST data where the last two bits of the quality control (QC) flags were equal to zero, and the CLM LST was selected by the rule that the MODIS LST was useful in the specified grid cell and specified time. Trend lines have been superimposed in the scatter plot of each moment.

At each instance when the satellite passed, the MODIS LST and CLM LST have a strong positive linear relationship. The Pearson's correlation coefficients are 0.9256, 0.9448, 0.8950, and 0.8669, respectively, and the P values are all less than 0.0001, which indicates the strong linear relationship. In other words, the CLM LST dataset shows a good agreement with the MODIS LST. Such agreement offers indirect proof of the availability of the CLM simulation results, since MODIS LST has been widely used in LST and UHI studies. Furthermore, it can be seen that the slopes of the trend lines are all less than 1, which indicates that the MODIS LST is always lower than the model simulation results. Some previous studies have shown that MODIS LST is underestimated in some regions (Li et al. 2014; Yu et al. 2014). If the same situation exists for the city of Xi'an, it can be concluded that although the model simulation results appear to overestimate the LST, they may in fact be closer to the true values. Therefore, in the following, the UHI is analyzed based on the model-simulated ground temperature.

The temporal variation of the UHI effect based on the CLM

The seasonal variation of the UHI effect The seasonal variation of UHII is shown in Fig. 6. The upper and lower boundaries of the blue box in Fig. 6 are the 25th percentile and the 75th percentile, respectively. The red line within the box marks the median value, and the ends of the whiskers above and below the box represent the maximum and minimum, which extend to the data point no more than 1.5 times the interquartile range (IQR) from the box. Moreover, the red points indicate the extreme data points which is upper than highest datum or lower than lowest datum. The ordered scores in the first box are made up of the average UHII at each instance (every 30 min) during the spring, and the other three ordered scores for the summer, autumn, and winter follow a similar regulation.

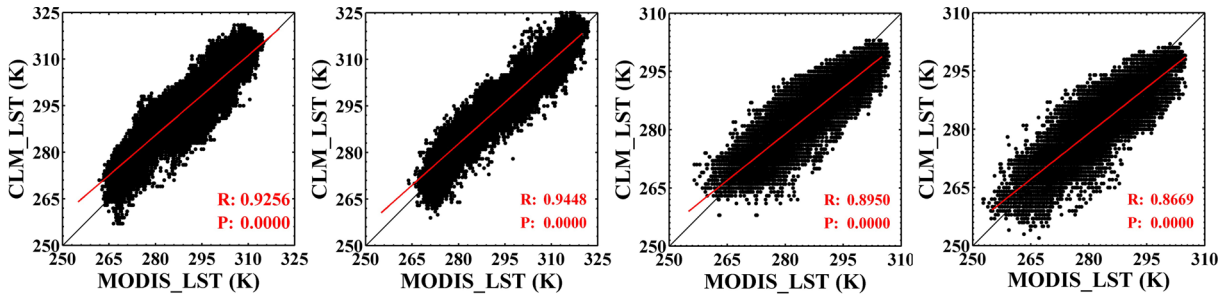

Fig. 5 Scatter plots of MODIS LST against CLM LST at the UTC times of **a** 02:30, **b** 05:30, **c** 14:30, and **d** 17:30, from March 1, 2003 to February 29, 2004. The red lines are the trend lines of each scatter plot, and the black lines are the 1:1 lines)

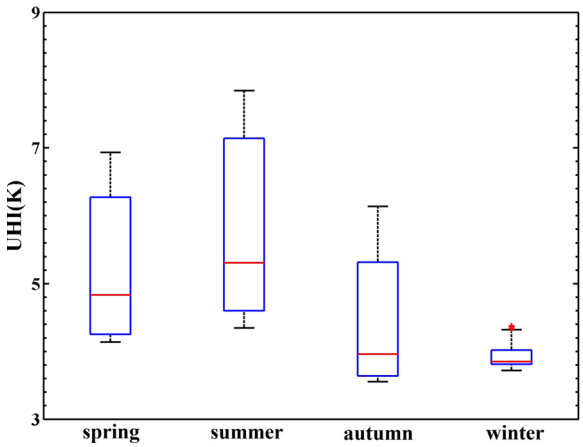

Fig. 6 Box and whisker plots of the seasonal variation of UHII from March 1, 2003 to February 29, 2004

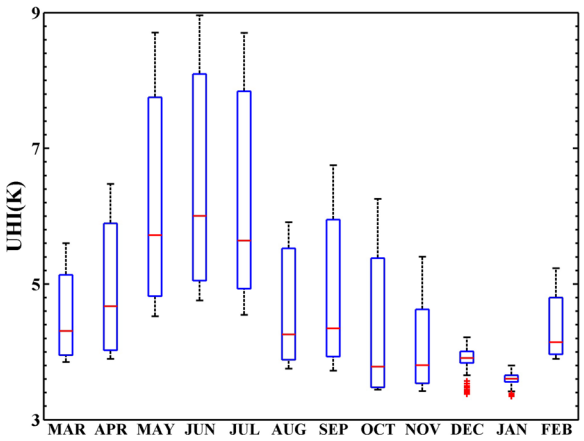

Fig. 7 Box and whisker plots of the monthly variation of UHII from March 1, 2003 to February 29, 2004

From Fig. 6, it can be seen that the intensity of the UHI effect in summer is the highest, followed by spring and autumn, while the urban heat stress in winter is the weakest in the whole year. Furthermore, the IQR in summer is the largest, while the IQR in winter is the shortest among the four seasons. This indicates that the UHI effect changes dramatically in the different hours of the day in summer, while the change trend becomes slower in winter. The median value shown as the red line in Fig. 6 in each season locates in the lower half of the box, which indicates that the number of weaker heat stress instances is more than the stronger heat stress instances.

The monthly variation of the UHI effect The monthly variation of UHII is shown in Fig. 7. The average diurnal cycle of UHII in each month contains 48 records because CLM4.5 outputted every 30 min in our simulation. Each box and whisker plot are composed of the 48 records in the corresponding month. The UHI effect reaches the highest level in June, where the maximum UHII is about 9 K, while the lowest monthly average UHII is less than 4 K in January. Taken as a whole, the UHI effect increases from January to June, and then decreases from June to the next January. However, fluctuations occur in August, corresponding with the overall trend of the monthly UHII change. The UHI effect in August is weaker than that in July and September.

In May, June, and July, the box plots are comparatively long, which indicates that the average diurnal UHII held quite different opinions about intensity in these months. Meanwhile, the box plots are comparatively short in December and January, which indicates that the average UHI effects have a high level of agreement with each other at the different times of the day during these months.

In addition, the lower values of the red points are under the lowest datum of whiskers in December and January, which reveals that a lot of the records in these two months are lower values. The median lines divide the boxes into two parts in the 12 box plots, and the upper parts are all larger than the lower parts; in other words, the number of stronger UHII values is less than that of the weaker UHII values. This phenomenon reveals that the urban areas are affected by relatively weak heat stress in most times of the day, while being affected by strong heat stress at certain times of the day.

The diurnal cycle of the UHI effect Figure 8 depicts the seasonal average diurnal cycle of ground temperature and UHII. It can be seen from Fig. 8a–d that the diurnal variation trends of the urban and rural ground temperature show a good agreement with each other in the four seasons. The ground temperature reaches a maximum at 06:30 a.m., while the minimum ground temperature in both the urban and rural areas appears between 22:00 to 24:00 p.m. UTC time.

The seasonal average diurnal cycle of UHII is shown in Fig. 8e–h. This is consistent with Fig. 6, in that the UHI effect is stronger in summer and weaker in winter, as indicated by the ordinate range of each sub-figure. The diurnal cycle trends of the

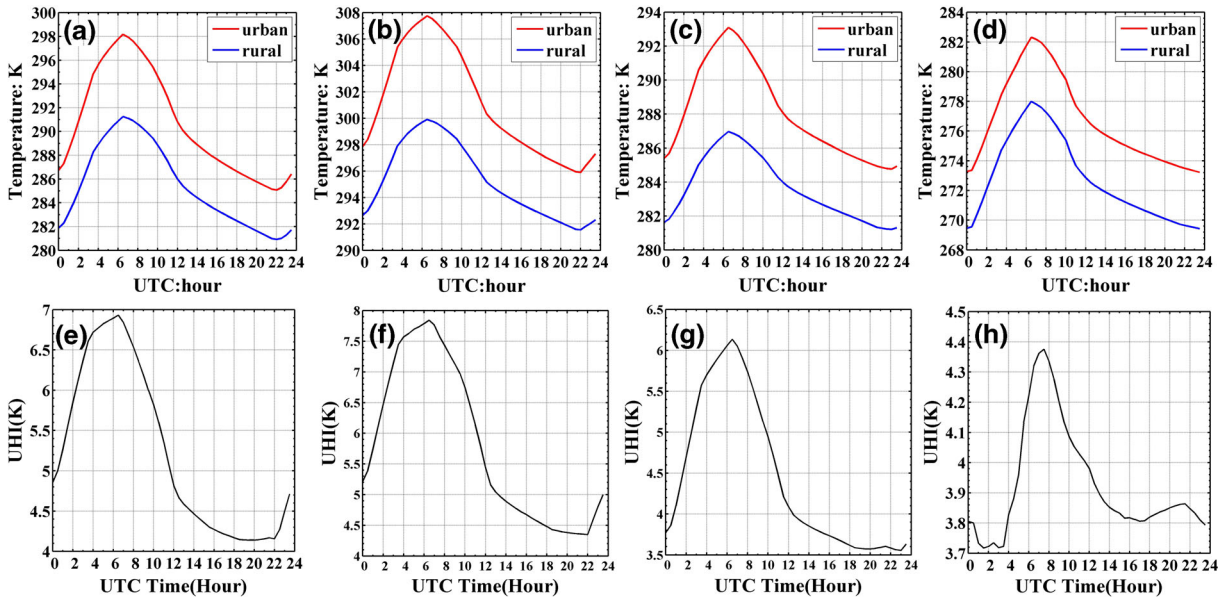

Fig. 8 The seasonal average diurnal cycle of ground temperature (**a**–**d**) and UHII (**e**–**h**) in spring (**a**, **e**), summer (**b**, **f**), autumn (**c**, **g**), and winter (**d**, **h**) (the red and blue lines in the upper four subgraphs indicate the average ground temperature over the urban area and rural area, respectively)

UHI effect have a high level of agreement with each other in spring, summer, and autumn, and all the seasons present a unimodal pattern with a significant peak at noon (around 6:30 a.m. UTC time). Although the winter has more than one peak, it is similar to the other seasons, with only one significant peak. To further understand the diurnal cycle of UHII, the diurnal variation characteristics of UHII based on the seasonal average diurnal cycle of the UHI datasets were summarized, and the results are shown in Table 1.

The second and third columns in Table 1 respectively represent the maximum and minimum UHII and their corresponding times. The last two columns are the mean values of UHII and the diurnal variation range of UHII in each season, respectively. For the seasonal variation trend of the maximum UHI effect, the highest value appears in summer, followed by spring and autumn, with the lowest value occurring in winter. The variation trends of both the minimum and mean UHI effect at the seasonal scale are similar to the maximum UHII. From the last column of Table 1, the diurnal cycle of the UHI effect varies in the range of 3.5373 K in summer, while the diurnal variation ranges of spring and autumn are 2.7923 and 2.5825 K, respectively. In contrast to the other seasons, the winter has a small diurnal variation range of UHII of 0.6581 K.

Table 1 Seasonal average diurnal cycle characteristics of UHII (K)

UHI	Max(UTC time)	Min(UTC time)	Mean	Max-Min
Spring	6.9323 (6:30)	4.1400 (19:30)	5.2293	2.7923
Summer	7.8448 (6:30)	4.3475 (22:00)	5.7929	3.5373
Autumn	6.1368 (6:30)	3.5543 (23:00)	4.4426	2.5825
Winter	4.3758 (7:30)	3.7177 (01:30)	3.9264	0.6581

Max means the maximum of UHII, *Min* means the minimum of UHII, *Mean* indicates the average UHII, *Max-Min* is calculated by Max minus Min

Furthermore, the intensity of the UHI effect in spring, summer, and autumn reaches the highest level at 06:30 a.m. UTC, while the hottest time comes an hour later in winter. The time of the minimum UHII pushes forward from spring to winter. Specifically, the difference between urban and rural ground temperature is at a minimum at 19:30 UTC in spring, while the minimum UHII appears at 22:00 in summer, then 1 h later in autumn, and the minimum appears at 01:30 in winter, with the weakest urban heat stress. On the whole, it can be seen from Fig. 8 and Table 1 that the intensity of the UHI effect rises from midnight or early morning to noon, and then decreases until the next midnight or morning.

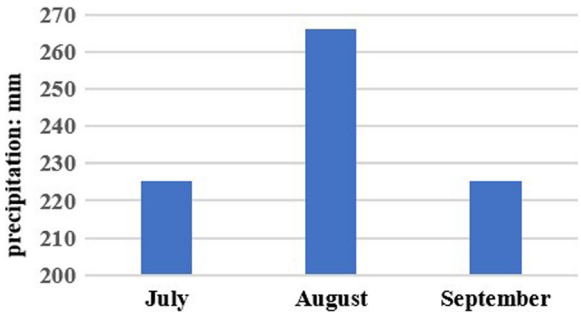

Fig. 9 The precipitation in Xi'an city in July, August, and September (JAS)

Discussion

According to the results, the UHII is stronger in summer than in winter. In summer, the land surface is always influenced by a high intensity of sunlight, and the impervious surfaces in the urban area absorb more heat, while the radiation in winter is lower than in the other seasons, and both the urban and rural areas are in a cold environment, which cannot store a lot of heat energy. In addition, the respiration and evaporation of vegetation may be another important factor that affects the UHI effect in the city of Xi'an, and the effect of the vegetation becomes weaker when it becomes withered.

As for the monthly variation of the UHI effect, the change curve is continuous. However, the UHI effect in August is lower than that in July and September. Generally speaking, the radiation and the weather conditions are similar in the three months; however, the UHII shows obvious differences. To further explain this phenomenon, we recorded the total precipitation in the three months, and the results are shown in Fig. 9. Table 2 summarizes and lists the various types of rain days and the total precipitation. The precipitation in August is obviously higher than that in July and September (Fig. 9). From Table 2, it can be seen that no matter the number of moderate rain days and excessively heavy rainfall days, August shows a significantly high value, despite the number of heavy rain days in August being less than those in July and September. A lot of rainfall may cause the decrease of the difference between urban and rural ground temperatures. The full rainfall can provide a better environment for vegetation growth. Furthermore, the evapotranspiration of vegetation significantly influences the ground temperature and urban heat island.

Table 2 The statistical characteristics of the precipitation in Xi'an city in July, August, and September (JAS)

	July	August	September
Total precipitation (mm)	225.1358	265.9508	225.1883
Moderate rain days	5	6	3
Heavy rain days	3	2	3
Excessively heavy rainfall days	0	1	0

In Xi'an city, the urban plant may grow luxuriantly under the condition of the sufficient water supply in August. Then the evaporation of urban vegetation has a good effect of cooling down the temperature. So the urban heat effect in August is weaker than in July and September. Previous studies (Ho et al. 2016; Peng et al. 2011) have also indicated that UHII has a significant negative correlation with the average precipitation in each season.

In winter, more than one peak exists in the diurnal cycle curve of UHII, which is not the case for the other seasons. To further confirm the results and analyze the reasons for this, the UHII in December, January, and February (DJF) of the winter months was calculated, respectively, and the results are shown in Fig. 10. The UHII in December and January varies over the range of 3.3 to 4.2 K in December and 3.3 to 3.8 K in January, respectively. Although the UHII has more than one peak and lots of lower values are contained in the two months, it shows a good agreement with the boxplot shown in Fig. 7. More specifically, the many low values existing in December and January cause the UHI jitter over a small range, thus forming several low peaks and only one high peak, which corresponds with the other months. To further investigate the phenomenon that intensity of UHI changes in a small range in winter, the diurnal changes of UHII in summer and winter are compared. The comparison results are shown in Fig. 11. From Fig. 11a, it can be seen that the UHII in summer months has an obvious continuous change in different hours of a day, especially in June and July. But in winter months as shown in Fig. 11b, the color representing UHII is very similar in different hours, especially in December and January. This phenomenon further indicates that the weak variation in winter formed the phenomenon that the winter diurnal cycle curve of UHII is different from other seasons.

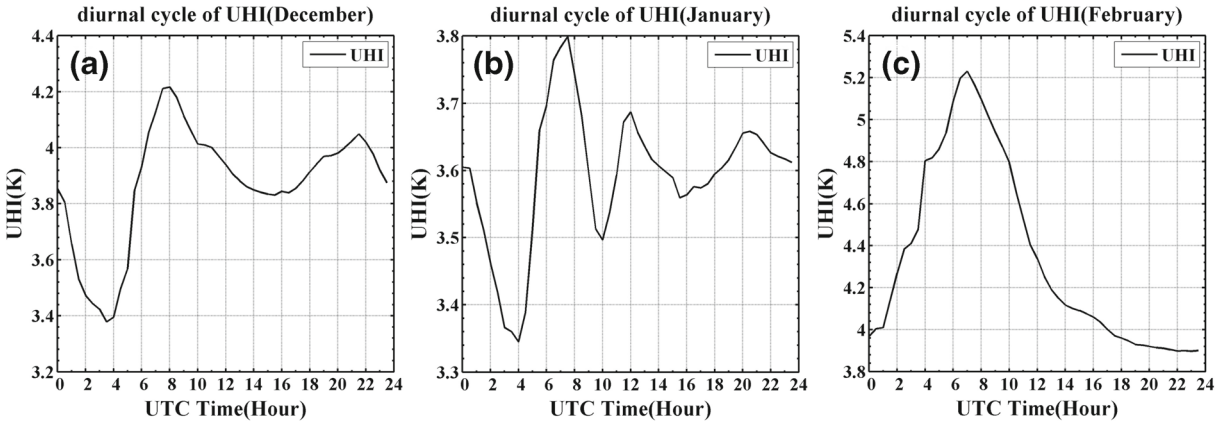

Fig. 10 The diurnal cycle of the UHI effect in **a** December, **b** January, and **c** February

As an important component of the environment, the UHI effect and its impact are crucial in our lives. The diurnal cycle of the UHI effect is related to the activities of humans. From the results of this study, we found that the diurnal variation of UHII is not very high in winter, while in summer, the gap between the minimum UHII and the maximum UHII at different times of the day reaches 3.5373 K. Based on the study results, it can be clearly seen that the diurnal cycle of the UHI effect in Xi'an generally shows a strong peak. The maximum UHI effect occurs in the period from 6:30 a.m. to 7:30 a.m. UTC time, which is close to the rush hour in Xi'an. This phenomenon may result in increased levels of heatstroke or other heat stress damage in the period when people are at their busiest. The maximum UHII occurs at midday, which is near the time of a high rate of travel. The study results could give direct suggestions about vehicle restrictions, and could provide a reference for policymakers about how to reduce the damage caused by heat stress.

The use of model simulation to study the UHI effect is a relatively new development; thus, in this study, we carried out a numerical simulation experiment to analyze the diurnal cycle of the UHI effect in the city of Xi'an. On the one hand, the model can not only provide a strong capability to study the UHI effect in

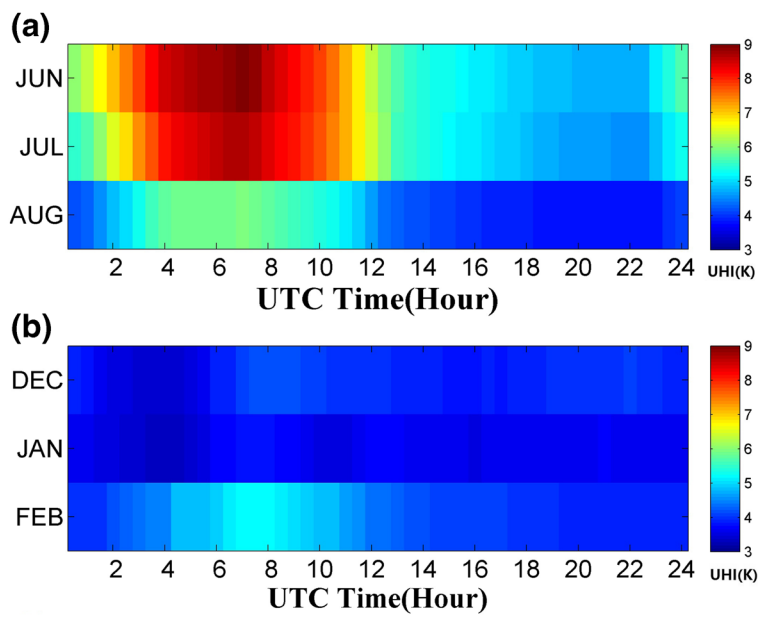

Fig. 11 The comparison of diurnal cycle of the UHI effect between summer (**a**) and winter (**b**)

a spatially and temporally continuous manner, but it has also been applied in the mechanism analysis of the UHI effect in some previous studies (Cao et al. 2016; Zhao et al. 2014). On the other hand, the simulation results are easily affected by many factors, such as the model forcing datasets, the model process description, the land-cover datasets, etc. As the accuracy of the remotely sensed LST is easily influenced by the retrieval algorithm and parameter settings, the model simulation results also contain some uncertainty. MODIS LST has been extensively used to study the UHI effect in many studies (Haashemi et al. 2016; Tran et al. 2006); thus, we compared CLM LST with MODIS LST. The results can provide the support for us to apply the model in UHI trend analysis, although accuracy uncertainty still exists in both the remotely sensed LST and the model simulation ground temperature.

Conclusions

In this study, a numerical simulation experiment for the city of Xi'an, China, from March 1, 2003 to February 29, 2004, based on CLM4.5 was conducted. The model simulation results were transferred to LST and then compared with MODIS LST. Based on the simulated spatially and temporally continuous ground temperature, the seasonal, monthly, and diurnal variations of the UHI effect were analyzed. According to the numerical simulation of the UHI effect based on CLM/CLMU, the following conclusions can be drawn:

1) The urban heat stress in summer is the strongest, followed by spring and autumn, and the UHI effect in winter is the weakest during the whole year.
2) The UHII reaches a maximum in July and decreases to a minimum in January.
3) Regarding the diurnal cycle of the UHI effect, the maximum UHI intensity appears at 06:30 a.m. UTC time in spring, summer, and autumn, and an hour later in winter. The minimum UHI intensity appears at 19:30, 22:00, 23:00, and 01:30 UTC time in spring, summer, autumn, and winter, respectively.
4) From the model simulation results, it can be seen that a significant peak in the diurnal cycle of UHII exists in each season, while more than one peak appears in winter, because the winter UHII varies over a small range.

Based on the results of this study, we know that the diurnal maximum UHII in Xi'an appears near the rush hour period. The results could provide guidelines for government policymakers about the response to heat stress damage. In our future studies, we will study the UHI effect over larger areas and at a finer spatial resolution, based on CLM4.5, to further study the main mechanisms and coping strategies for the UHI effect.

Acknowledgements This work was supported by the National Natural Science Foundation of China (41422108, 41661134015); Cross-disciplinary Collaborative Teams Program for Science, Technology and Innovation of the Chinese Academy of Sciences.

References

Aikawa, M., Hiraki, T., Eiho, J., Miyazaki, H. (2007). Characteristic air temperature distributions observed in summer and winter in urban area in Japan. *Environmental Monitoring and Assessment*, *131*(1), 255–265.

Anderson, M., Norman, J., Kustas, W., Li, F., Prueger, J., Mecikalski, J. (2005). Effects of vegetation clumping on two–source model estimates of surface energy fluxes from an agricultural landscape during smacex. *Journal of Hydrometeorology*, *6*(6), 892–909.

Bowling, S. (1983). *Meteorological factors responsible for high CO levels in Alaskan cities*. Environmental Research Laboratory, Office of Research and Development, US Environmental Protection Agency.

Cao, C., Lee, X., Liu, S., Schultz, N., Xiao, W., Zhang, M., Zhao, L. (2016). Urban heat islands in China enhanced by haze pollution. *Nature Communications*, 7, 12509.

Chen, X., Zhao, H., Li, P., Yin, Z. (2006). Remote sensing image-based analysis of the relationship between urban heat island and land use/cover changes. *Remote Sensing of Environment*, *104*(2), 133–146.

Chen, Y., Yang, K., He, J., Qin, J., Shi, J., Du, J., He, Q. (2011). Improving land surface temperature modeling for dry land of China. *Journal of Geophysical Research: Atmospheres, 116*(D20), 104.

Chow, W., & Roth, M. (2006). Temporal dynamics of the urban heat island of singapore. *International Journal of Climatology*, *26*(15), 2243–2260.

Du, H., Wang, D., Wang, Y., Zhao, X., Qin, F., Jiang, H., Cai, Y. (2016). Influences of land cover types, meteorological conditions, anthropogenic heat and urban area on surface urban heat island in the yangtze river delta urban agglomeration. *Science of the Total Environment*, *571*, 461–470.

Gent, P., Danabasoglu, G., Donner, L., Holland, M., Hunke, E., Jayne, S., Lawrence, D., Neale, R., Rasch, P., Vertenstein,

M., et al. (2011). The community climate system model version 4. *Journal of Climate*, *24*(19), 4973–4991.

Giannaros, T., Melas, D., Daglis, I., Keramitsoglou, I., Kourtidis, K. (2013). Numerical study of the urban heat island over athens (greece) with the wrf model. *Atmospheric Environment*, *73*, 103–111.

Haashemi, S., Weng, Q., Darvishi, A., Alavipanah, S. (2016). Seasonal variations of the surface urban heat island in a semi-arid city. *Remote Sensing*, *8*(4), 352.

Ho, H., Knudby, A., Xu, Y., Hodul, M., Aminipouri, M. (2016). A comparison of urban heat islands mapped using skin temperature, air temperature, and apparent temperature (humidex), for the greater vancouver area. *Science of the Total Environment*, *544*, 929–938.

Iodice, P., & Senatore, A. (2012). *Analysis of a scooter emission behavior in cold and hot conditions: modelling and experimental investigations*. SAE Technical Paper.

Iodice, P., & Senatore, A. (2013). Road transport emission inventory in a regional area by using experimental two-wheelers emission factors. In *Lectures notes in engineering and computer sciences: proceedings of the world congress on engineering* (pp. 681–685).

Iodice, P., & Senatore, A. (2015). Appraisal of pollutant emissions and air quality state in a critical italian region: Methods and results. *Environmental Progress and Sustainable Energy*, *34*(5), 1497–1505.

Jackson, T., Feddema, J., Oleson, K., Bonan, G., Bauer, J. (2010). Parameterization of urban characteristics for global climate modeling. *Annals of the Association of American Geographers*, *100*(4), 848–865.

Kustas, W., & Anderson, M. (2009). Advances in thermal infrared remote sensing for land surface modeling. *Agricultural and Forest Meteorology*, *149*(12), 2071–2081.

Lawrence, D., Oleson, K., Flanner, M., Thornton, P., Swenson, S., Lawrence, P., Zeng, X., Yang, Z., Levis, S., Sakaguchi, K., et al. (2011). Parameterization improvements and functional and structural advances in version 4 of the community land model. *Journal of Advances in Modeling Earth Systems, 3*(1), M03001.

Li, H., Sun, D., Yu, Y., Wang, H., Liu, Y., Liu, Q., Du, Y., Wang, H., Cao, B. (2014). Evaluation of the viirs and modis lst products in an arid area of Northwest China. *Remote Sensing of Environment*, *142*, 111–121.

Magee, N., Curtis, J., Wendler, G. (1999). The urban heat island effect at fairbanks, Alaska. *Theoretical and Applied Climatology*, *64*(1), 39–47.

Meehl, G., & Tebaldi, C. (2004). More intense, more frequent, and longer lasting heat waves in the 21st century. *Science*, *305*(5686), 994–997.

Miao, S., Chen, F., LeMone, M.A., Tewari, M., Li, Q., Wang, Y. (2009). An observational and modeling study of characteristics of urban heat island and boundary layer structures in Beijing. *Journal of Applied Meteorology and Climatology*, *48*(3), 484–501.

Ohashi, Y., Genchi, Y., Kondo, H., Kikegawa, Y., Yoshikado, H., Hirano, Y. (2007). Influence of air-conditioning waste heat on air temperature in tokyo during summer: numerical experiments using an urban canopy model coupled with a building energy model. *Journal of Applied Meteorology and climatology*, *46*(1), 66–81.

Oke, T. (1995). The heat island of the urban boundary layer: characteristics, causes and effects. In *Wind climate in cities* (pp. 81–107): Springer.

Oleson, K., Bonan, G., Feddema, J., Vertenstein, M., Kluzek, E. (2010a). *Technical description of an urban parameterization for the community land model (clmu)*. Boulder: NCAR.

Oleson, K., Lawrence, D., Gordon, B., Flanner, M., Kluzek, E., Peter, J., Levis, S., Swenson, S., Thornton, E., Feddema, J., et al. (2010b). *Technical description of version 4.0 of the community land model (clm)*. Boulder: NCAR.

Oleson, K., Bonan, G., Feddema, J., Jackson, T. (2011). An examination of urban heat island characteristics in a global climate model. *International Journal of Climatology*, *31*(12), 1848–1865.

Oleson, K., Lawrence, D., Bonan, G., Drewniak, B., Huang, M., Koven, C., Levis, S., Li, F., Riley, W., Subin, Z., Swenson, S., Thornton, P. (2013). *Technical description of version 4.5 of the community land model (clm)*. Boulder: NCAR.

Oleson, K., Monaghan, A., Wilhelmi, O., Barlage, M., Brunsell, N., Feddema, J., Hu, L., Steinhoff, D. (2015). Interactions between urbanization, heat stress, and climate change. *Climatic Change*, *129*(3–4), 525–541.

Peng, S., Piao, S., Ciais, P., Friedlingstein, P., Ottle, C., Breon, F., Nan, H., Zhou, L., Myneni, R. (2011). Surface urban heat island across 419 global big cities. *Environmental Science & Technology*, *46*(2), 696–703.

Rizwan, A., Dennis, L., Chunho, L. (2008). A review on the generation, determination and mitigation of urban heat island. *Journal of Environmental Sciences*, *20*(1), 120–128.

Saaroni, H., Ben-Dor, E., Bitan, A., Potchter, O. (2000). Spatial distribution and microscale characteristics of the urban heat island in tel-aviv, Israel. *Landscape and Urban Planning*, *48*(1), 1–18.

Salamanca, F., Martilli, A., Yagüe, C. (2012). A numerical study of the urban heat island over madrid during the desirex (2008) campaign with wrf and an evaluation of simple mitigation strategies. *International Journal of Climatology*, *32*(15), 2372–2386.

Shen, H., Li, X., Cheng, Q., Zeng, C., Yang, G., Li, H., Zhang, L. (2015). Missing information reconstruction of remote sensing data: a technical review. *IEEE Geoscience and Remote Sensing Magazine*, *3*(3), 61–85.

Shen, H., Huang, L., Zhang, L., Wu, P., Zeng, C. (2016a). Long-term and fine-scale satellite monitoring of the urban heat island effect by the fusion of multi-temporal and multi-sensor remote sensed data: a 26-year case study of the city of wuhan in china. *Remote Sensing of Environment*, *172*, 109–125.

Shen, H., Meng, X., Zhang, L. (2016b). An integrated framework for the spatio-temporal-spectral fusion of remote sensing images. *IEEE Transactions on Geoscience and Remote Sensing*, *54*(12), 7135–7148.

Smith, D., Cusack, S., Colman, A., Folland, C., Harris, G., Murphy, J. (2007). Improved surface temperature prediction for the coming decade from a global climate model. *Science*, *317*(5839), 796–799.

Sun, D., & Pinker, R. (2003). Estimation of land surface temperature from a geostationary operational environmental

satellite (goes-8). *Journal of Geophysical Research: Atmospheres, 108*(D11), 4326.

Tran, H., Uchihama, D., Ochi, S., Yasuoka, Y. (2006). Assessment with satellite data of the urban heat island effects in asian mega cities. *International Journal of Applied Earth Observation and Geoinformation*, *8*(1), 34–48.

Viovy, N. (2011). Cruncep dataset. http://dods.extra.cea.fr/data/p529viov/cruncep/readme.htm, http://dods.extra.cea.fr/store/p529viov/cruncep/V4_1901_2011/. Accessed: 10 August 2013.

Voogt, J., & Oke, T. (2003). Thermal remote sensing of urban climates. *Remote sensing of environment*, *86*(3), 370–384.

Wan, Z. (2014). New refinements and validation of the collection-6 modis land-surface temperature/emissivity product. *Remote Sensing of Environment*, *140*, 36–45.

Wan, Z., Zhang, Y., Zhang, Q., Li, Z. (2004). Quality assessment and validation of the modis global land surface temperature. *International Journal of Remote Sensing*, *25*(1), 261–274.

Weng, Q. (2009). Thermal infrared remote sensing for urban climate and environmental studies: methods, applications, and trends. *ISPRS Journal of Photogrammetry and Remote Sensing*, *64*(4), 335–344.

Weng, Q., & Fu, P. (2014). Modeling diurnal land temperature cycles over los angeles using downscaled goes imagery. *ISPRS Journal of Photogrammetry and Remote Sensing*, *97*, 78–88.

Xu, S. (2009). An approach to analyzing the intensity of the daytime surface urban heat island effect at a local scale. *Environmental Monitoring and Assessment*, *151*(1), 289–300.

Yang, K., He, J., Tang, W., Qin, J., Cheng, C.C. (2010). On downward shortwave and longwave radiations over high altitude regions: Observation and modeling in the tibetan plateau. *Agricultural and Forest Meteorology*, *150*(1), 38–46.

Yu, W., Ma, M., Wang, X., Geng, L., Tan, J., Shi, J. (2014). Evaluation of modis lst products using longwave radiation ground measurements in the northern arid region of China. *Remote Sensing*, *6*(11), 11,494–11,517.

Yuan, F., & Bauer, M. (2007). Comparison of impervious surface area and normalized difference vegetation index as indicators of surface urban heat island effects in landsat imagery. *Remote Sensing of Environment*, *106*(3), 375–386.

Zakšek, K., & Oštir, K. (2012). Downscaling land surface temperature for urban heat island diurnal cycle analysis. *Remote Sensing of Environment*, *117*, 114–124.

Zhang, K., Wang, R., Shen, C., Da, L. (2010). Temporal and spatial characteristics of the urban heat island during rapid urbanization in Shanghai, China. *Environmental Monitoring and Assessment*, *169*(1), 101–112.

Zhang, H., Jin, M., Leach, M. (2017). A study of the oklahoma city urban heat island effect using a wrf/single-layer urban canopy model, a joint urban 2003 field campaign, and modis satellite observations. *Climate, 5*(3), 72.

Zhao, L., Lee, X., Smith, R.B., Oleson, K. (2014). Strong contributions of local background climate to urban heat islands. *Nature*, *511*(7508), 216–219.